

## Spontaneous self-propulsion and nonequilibrium shape fluctuations of a droplet enclosing active particles

Gašper Kokot<sup>1,2,3</sup>, Hammad A. Faizi<sup>4</sup>, Gerardo E. Pradillo<sup>4</sup>, Alexey Snezhko<sup>2</sup> & Petia M. Vlahovska<sup>1</sup>   

Active particles, such as swimming bacteria or self-propelled colloids, spontaneously assemble into large-scale dynamic structures. Geometric boundaries often enforce different spatio-temporal patterns compared to unconfined environment and thus provide a platform to control the behavior of active matter. Here, we report collective dynamics of active particles enclosed by soft, deformable boundary, that is responsive to the particles' activity. We reveal that a quasi two-dimensional fluid droplet enclosing motile colloids powered by the Quincke effect (Quincke rollers) exhibits strong shape fluctuations with a power spectrum consistent with active fluctuations driven by particle-interface collisions. A broken detailed balance confirms the nonequilibrium nature of the shape dynamics. We further find that rollers self-organize into a single drop-spanning vortex, which can undergo a spontaneous symmetry breaking and vortex splitting. The droplet acquires motility while the vortex doublet exists. Our findings provide insights into the complex collective behavior of active colloidal suspensions in soft confinement.

<sup>1</sup> Engineering Sciences and Applied Mathematics, Northwestern University, Evanston, IL 60208, USA. <sup>2</sup> Materials Science Division, Argonne National Laboratory, Lemont, IL 60439, USA. <sup>3</sup> Institute for Biophysics, Medical Faculty, University of Ljubljana, Vrazov trg 2, Ljubljana 1000, Slovenia. <sup>4</sup> Mechanical Engineering, Northwestern University, Evanston, IL 60208, USA.  email: [petia.vlahovska@northwestern.edu](mailto:petia.vlahovska@northwestern.edu)

**A**ctive (self-driven) particles such as motile colloids present novel opportunities for the engineering of smart materials that can self-heal or change properties on demand<sup>1,2</sup>. The reconfigurability of active materials stems from the propensity of active particles to self-organize into large-scale dynamic structures that can be modulated by external cues such as electric or magnetic fields<sup>3–10</sup>, light<sup>11,12</sup>, or chemical reactions<sup>13–15</sup>. The spatio-temporal patterns can be also manipulated by geometric boundaries. For example, while unconfined suspensions of bacteria exhibit turbulent-like flow<sup>16–19</sup>, confinement into a long and narrow macroscopic “racetrack” geometry stabilizes bacterial motion into a steady unidirectional circulation<sup>20,21</sup>, and when subjected to 2D arrays of vertical pillars arranged in a square pattern bacterial suspensions transforms into a lattice of hydrodynamically bound vortices with a long-range antiferromagnetic order<sup>22</sup>. Inside of a droplet, the bacteria form a macro-scale bidirectional vortex<sup>23,24</sup>. Similar behaviors are also observed with synthetic microswimmers. For example, the Quincke rollers, which are powered by a spontaneous electro-rotation of a dielectric sphere exposed to a static electric field, self-organize into a long, polar band and undergo directional motion in the racetrack microfluidic channel<sup>25</sup>, while in strong confinement (rectangular geometries), the band state is replaced by a single macroscopic vortex<sup>26</sup>.

A confinement that is responsive to the particles activity adds another degree of freedom that can unlock novel collective states and dynamics. Active matter confined in drops can exhibit spontaneous symmetry breaking<sup>27,28</sup> leading to droplet motility<sup>29,30</sup>. Active droplets also mimic cell behaviors such as growth, division, and reshaping<sup>31,32</sup>. Bacteria and self-propelled colloids encapsulated in a droplet or a vesicle (bilayer membrane sac) drive strong shape deformations<sup>32–35</sup> and can cause net motion<sup>33,36–40</sup>.

Here, we explore the relation between the particle’s activity, deformations and motility of the soft confining container. As active particles we employ the Quincke rollers since their speed and locomotion pattern can be easily manipulated<sup>41,42</sup>. We use a soft container comprised of a liquid droplet sandwiched between two electrodes, which creates quasi two-dimensional geometry. We find that at low activity (quantified by the speed of the rollers) the droplet contour fluctuates, while the droplet stays nearly stationary, and the rollers self-organize into a vortex spanning the whole system. Increasing the activity leads to a growth of the shape fluctuations that exhibit a power spectrum consistent with active fluctuations driven by particle-interface collisions. Coupling of activity and soft boundary fluctuations often results in bursts of the droplet translation in a randomly selected direction. The net propulsion is driven by a spontaneous formation of a vortex doublet composed of two counter-rotating vortices.

## Results

**Particle dynamics inside the droplet.** The experimental system consists of 40  $\mu\text{m}$  polystyrene spheres dispersed in hexadecane/AOT medium (see “Methods” section for details). A small volume of the solution (approx. 5  $\mu\text{L}$ ) is sandwiched between two indium tin oxide (ITO) coated glass electrodes spaced 150  $\mu\text{m}$  apart to form a liquid bridge with a high aspect ratio that produces a quasi-two-dimensional droplet (Figs. 1a and 2a). The particles are allowed to sediment on the bottom electrode before the application of a uniform DC electric field  $E$  between the electrodes. Above a threshold magnitude  $E_{\text{Q}}$  particles develop a steady rotation due to the Quincke effect<sup>25,43</sup> (see Supplementary note I for an overview of the phenomenon) and start to roll on the bottom surface.

Hydrodynamic and electrostatic interactions between the rollers promote alignment of their translational directions and

result in a formation of multiple transient flocks and vortices of particles (Fig. 1b, c). Eventually, multiple vortices and flocks merge to form a macroscopic global vortex inside the droplet, see Fig. 2b, c. Similarly to vortices formed by magnetic rollers<sup>44,45</sup>, the vortex spontaneously selects its handedness (clockwise or counterclockwise) that changes from experiment to experiment. The particles velocity fields in the droplet reveal a dramatic change in its appearance compared to rollers confined by a solid boundary<sup>26</sup>, where the rollers accumulate near the confining interface. In the droplet system, the rollers are distributed throughout the droplet interior being more packed in the center of the droplet and less densely packed towards the drop edge. This is most clearly seen in Fig. 2c as one bright blur in the center of the droplet—a big crowd of rollers rotating as one vortex—and several bright blurs around—flocks orbiting in the direction of the rotation. Equal direction of rotation for the whole system is confirmed by a single central peak in the vorticity field of Fig. 2c. For comparison, in Fig. 2b, where the system is in the intermediate state, there are several large off-center bright blurs—crowds of rollers creating vortical flows with clock or counterclockwise as illustrated by the local minima and a maxima in the vorticity field of Fig. 2b (for a closer inspection see Supplementary Movie 2). The different structure of the vortex confined by solid and soft boundary likely results from interface deformability and mobility. The droplet shape constantly fluctuates and even if the deformations are small, they may be sufficiently strong to push rollers away from the boundary.

The equilibrium droplet contour in the absence of activity (below the onset of Quincke rotation) is a circle (Fig. 2a). Once the rollers become motile, the interface begins to fluctuate and during the process of vortex formation the droplet shape can become very non-circular (see Fig. 2b and Supplementary Movie 1). Even when the vortex is formed the shape continues to fluctuate (see Fig. 2c, Supplementary Movie 2, and Supplementary Fig. S1). We quantify the droplet deformations by the asphericity parameter  $\Delta$  (see “Methods” section), with  $\Delta = 0$  corresponding to a perfect circle. Figure 2d shows that once the system is energized, the droplet undergoes pronounced shape deformations until a macroscopic vortex is formed and  $\Delta$  decreases back to nearly pre-activation values (nevertheless shape fluctuations are still present). The gradual growth of the macroscopic vortex is illustrated by a correlation length,  $r_{\text{corr}}$  defined as the first zero crossing of the spatial velocity correlation function,  $C_{\text{norm}}(r)$  (Fig. 2d inset).  $r_{\text{corr}}$  exhibits a monotonic growth while the individual rollers organize into flocks and transient vortices (the velocity fluctuations phase), and it reaches a plateau when the globally correlated state (vortex) is formed.

**Nonequilibrium shape fluctuations.** The shape of the active droplet undergoes strong fluctuations with amplitude reaching 10–15% of the initial droplet radius, see Fig. 3a. The deviation from the equilibrium circular shape,  $h(s, t) = r_s(s, t) - R_{\text{drop}}$ , where  $r_s$  is the droplet interface position at arclength  $s$ , is fitted with Fourier series,  $h(s, t) = \sum h_q(t) \exp(iqs)$  (see “Methods” section). The power spectrum of the shape fluctuations exhibits a power-law dependence on wavenumber  $q$ ,  $\langle |h_q|^2 \rangle \sim q^{-4}$  (Fig. 3b). Thermal fluctuations of the droplet interface would exhibit a power spectrum with  $q^{-2}$  capillary scaling for surface-tension-controlled shape relaxation, suggestive that the origin of the fluctuations is non-equilibrium.

The temporal behavior of the shape fluctuations also indicates out-of-equilibrium dynamics. In the active state, the relaxation time obtained from the time autocorrelation function,  $\langle h_q(0) h_q^*(t) \rangle = \langle |h_q|^2 \rangle \exp\left(-\frac{t}{\tau_q}\right)$ , displays a power-law decay with  $q$  with exponent close to  $-3/2$ , see Fig. 3c. In equilibrium

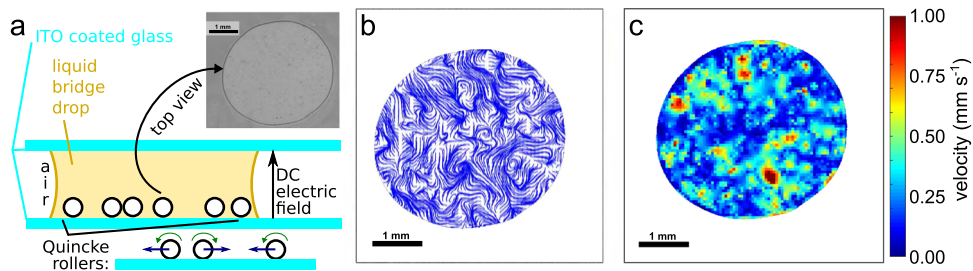


**Fig. 1 Quincke rollers in a droplet.** **a** A sketch of the experimental system: A small amount of weakly conductive liquid (hexadecane) surrounded by air forms a bridge between two planar electrodes. Inside of the quasi-two-dimensional drop are polystyrene spheres that start to roll upon application of a uniform DC electric field,  $E$ . Quincke rollers initially move in random directions along the surface of the bottom electrode. Blue and green arrows indicate the direction of translation and rotation of the rollers, respectively. The image shows the top view of the drop and enclosed rollers. **b** The monolayer of rolling particles generates an essentially two dimensional flow. Streamlines reveal the formation of transient vortices throughout the droplet. **c** Snapshot of the velocity field inside the droplet as determined by particle image velocimetry (PIV). Experimental parameters: packing fraction of the Quincke rollers  $\varphi = 0.58 \pm 0.11$ , droplet area is  $A_{\text{drop}} = 11.05 \pm 0.03 \text{ mm}^2$ , the driving electric field  $E = 3.193 \pm 0.007 \text{ MV m}^{-1}$ .

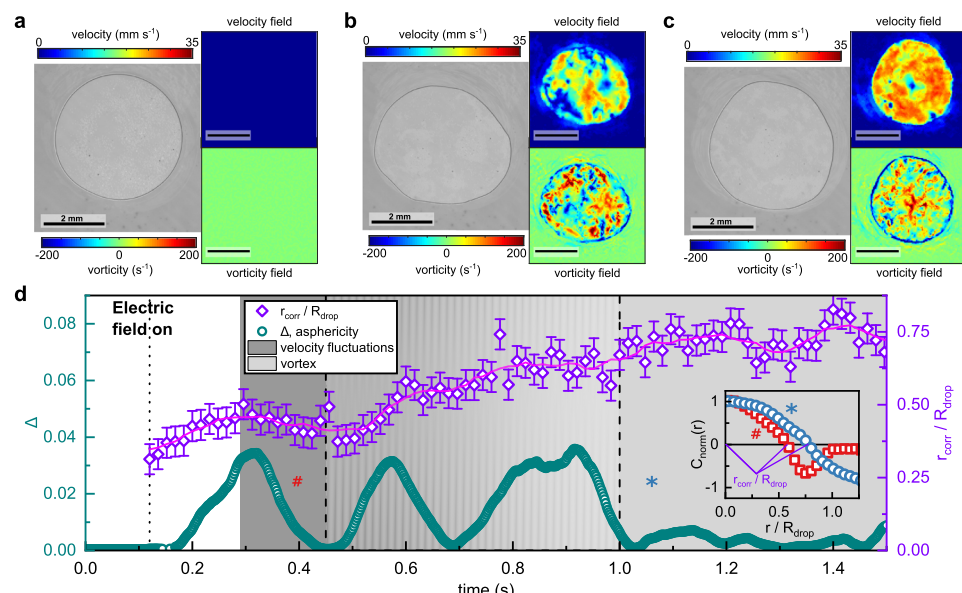


**Fig. 2 Shape fluctuations of a droplet enclosing Quincke rollers.** **a** A droplet in the absence of the electric field,  $E = 0$ . **b** Regime of transient flocks and vortices (velocity fluctuations phase). Rollers velocity and vorticity fields in the droplet. Both clockwise (blue) and counter-clockwise (red) vorticity is simultaneously present indicative of transient vortices. Even though the time-variation of the asphericity  $\Delta$  appears periodic, this behavior is specific for this particular experiment and it is not universally observed. **c** Globally correlated state (vortex phase). Velocity and vorticity fields indicate the presence of a single macroscopic vortex. **d** Evolution of the droplet shape characterized by the asphericity,  $\Delta$  (cyan circles, left scale). The right scale presents the time evolution of the correlation length  $r_{\text{corr}}$  on the same dataset, as defined in the inset from  $C_{\text{norm}}(r)$ , the normalized spatial correlation of velocity field, first zero crossing, normalized by the drop radius  $R_{\text{drop}}$ . The inset shows  $C_{\text{norm}}(r)$  computed from the data in the velocity fluctuations (#) and vortex (\*) phases. The dashed lines delineate the regimes of velocity fluctuations, transition to vortex, and developed vortex. The error bars are the standard error of the mean and the purple line is a running average of the data points to guide the eye. When error bars are not visible they are smaller than the symbols. Experimental parameters: rollers packing fraction  $\varphi = 0.18 \pm 0.04$ , droplet area  $A_{\text{drop}} = 13.56 \pm 0.03 \text{ mm}^2$  and electric field strength  $E = 5.104 \pm 0.008 \text{ MV m}^{-1}$ .

systems, thermal shape fluctuations with mean-squared amplitude  $\sim q^{-4}$  are exhibited by bilayer membranes and semiflexible polymers and are due to bending rigidity. The bending forces drive relaxation with rates  $\sim q^3$  for membranes and  $\sim q^4$  for polymers<sup>46–48</sup>. However, in non-equilibrium systems the excitation and relaxation need not to have same driving forces. The  $q^{-4}$ -law of the power spectrum is observed for vesicle shape fluctuations due to particle-interface collisions<sup>32,35</sup> and active ring polymer<sup>49</sup>. In the latter system, the relaxation times are predicted to be  $\sim q^{-2}$  and  $q^{-4}$  for tension and bending controlled modes, respectively. In our system, the fluctuations are driven by the strong flows generated by the Quincke rollers. The deformations are opposed by the surface tension and the relaxation rates are set by dissipation

due to the motion of the contact line<sup>50,51</sup>. An estimate based on the balance of surface tension  $\gamma$  and viscous dissipation by viscosity  $\mu$  gives for the relaxation time  $\tau_q = \mu / \gamma \theta^3 q$ , where  $\theta$  is the contact angle<sup>50</sup>. This  $1/q$  dependence of relaxation time is weaker than the experimentally observed one, suggesting that the relaxation is not purely driven by contact line elasticity and likely impacted by the activity.

To quantify the non-equilibrium nature of the fluctuations, we test for broken detailed balance in the transitions between microscopic configurations<sup>52</sup> (see “Methods” section). The configurations correspond to the shapes defined by different Fourier modes. In equilibrium, it is equally likely for the forward and backward transition to occur between any two different

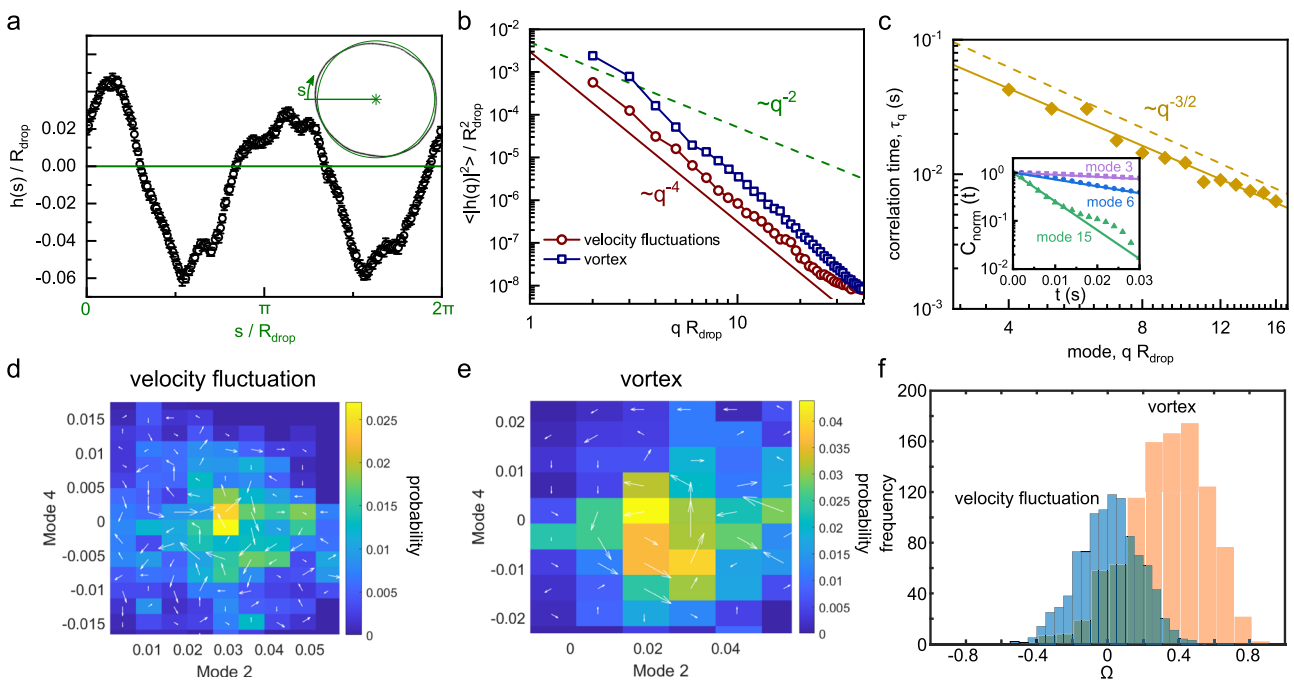


**Fig. 3 Analysis of the shape fluctuations.** **a** A snapshot of the contour  $h$  around the equivalent circle radius  $R_{\text{drop}}$ . The coordinate  $s$  runs along the circumference of the equivalent circle (inset, green). The liquid-air interface is deformed (inset, black) by the activity inside the droplet and deviates from  $R_{\text{drop}}$  by  $h$ . **b** A time-averaged power spectrum  $\langle |h_q|^2 \rangle$  dependence on the wave number  $q$  for two cases: fluctuating velocity regime and fully developed vortex regime. In both cases the decay of the power spectrum falls off as  $q^{-4}$ . **c** Relaxation time of the autocorrelations as a function of the wavenumber  $q$ . The inset shows the autocorrelation functions for three modes. The fit of the data results in power law with exponent  $\simeq -3/2$  shown as a dashed line (the exact fit gives the exponent  $-1.41 \pm 0.08$  shown as a solid line). **d, e** Probability distribution (color) and flux map (arrows) in phase space spanned by Fourier modes 2 and 4 in **d** the velocity fluctuation and **e** vortex phases. Arrows length corresponds to the magnitude of the fluxes. The plots for the other modes are shown on Supplementary Fig. S6 and Fig. S7. **f** The contour integral of the probability current,  $\Omega$ , histograms for **d, e** show different values in the velocity fluctuations phase (blue,  $\Omega = 0.01 \pm 0.17$ ) and vortex phase (orange,  $\Omega = 0.32 \pm 0.22$ ). Error bars are the standard error of the mean. In **b, c** error bars are smaller than the symbols.

Fourier modes. A non-equilibrium system, however, would display a probability flux in the phase space of shapes. Figure 3d, e show the probability density map for two Fourier modes of the fluctuating droplet. The probability is defined as the ratio of the time spent at a given state. The arrows indicate the currents across box boundaries determined by counting transitions between boxes. A nonzero value of the contour integral of the probability current,  $\Omega = \frac{\oint_C j \cdot d\ell}{\oint_C |j| d\ell}$ , indicates out of equilibrium dynamics (Fig. 3f). The broken detailed balance analysis also reveals that the modes gradually go out of equilibrium, starting with the short wavelengths. The longest wavelength modes are in equilibrium early in the velocity fluctuation phase (Fig. 3d, f) and become nonequilibrium in the vortex phase (Fig. 3e, f). This reflects the structure evolution: rollers cluster into aggregates with growing size that eventually become the droplet-spanning vortex.

**Activity enhancement of the shape fluctuations.** Thermally-driven droplet shape fluctuations are negligible in our system due to strong surface tension. For an oil/air interface the surface tension is  $\gamma = 10 \text{ mN m}^{-1}$ , which corresponds to interfacial energy far exceeding the thermal energy,  $\sim 10^{12} k_B T$ , for a droplet with radius of 1 mm; the amplitude of the fluctuations calculated from  $\langle |h_q|^2 \rangle = k_B T / \gamma q^2 L^2$ , where the contour length is  $L = 2\pi R_{\text{drop}}$ , is below a nanometer even for the lowest wavemode. However, in the active state the rollers generate flows that can be strong enough to overcome surface tension and deform the interface. An individual roller with radius  $a$  moves with speed  $a\dot{G}$ , where the generated flow strain rate is  $\dot{G} = \tau_{\text{mw}}^{-1} \sqrt{(E/E_Q)^2 - 1}$  (see SI for

details). In our system, the Maxwell-Wagner time is  $\tau_{\text{mw}} \sim 1 \text{ ms}$ . The flow can exert stress on the interface in the order of  $\mu\dot{G} \sim 1 \text{ Pa}$ , which is comparable to the capillary stress  $\gamma q$ . Since the flow is created by the rollers, the active shape fluctuations are expected to increase if either the rollers velocity or number increases.

To quantify the effects of the activity, we define an effective energy of the system from velocity fluctuations<sup>53</sup>

$$U = \frac{1}{2} \sum_N m_N u_N^2 \quad (1)$$

where the index  $N$  runs over the individual rollers, and  $\mathbf{u}_N = \mathbf{v}_N - \mathbf{v}$  is the difference between the individual roller velocity,  $\mathbf{v}_N$ , and the macroscopic flow,  $\mathbf{v}$ . Experimentally, however, we have access neither to the individual particle trajectories nor the detailed hydrodynamic flow, therefore we consider  $\mathbf{v}$  to be the instantaneous velocity of the droplet center and  $\mathbf{v}_N$  the velocity field pixel from PIV velocity fields of the particles. PIV procedure is based on image contrast correlations and detects only the movement of the particles in the droplet making the velocity field a good approximation for the actual particle velocities as long as the packing fraction  $\varphi$  is large. Assuming that all particles have equal mass  $m_N = m_p$  and replacing the summation by the temporal average value of the square of the velocity fluctuations  $\langle u_N^2 \rangle$  yields for the energy density

$$e = U/A_{\text{droplet}} = \frac{2}{3} \varphi \rho \langle u_N^2 \rangle, \quad (2)$$

where  $\rho$  is the buoyant density of particles. In our system the velocity of individual particles depends on the driving electric field

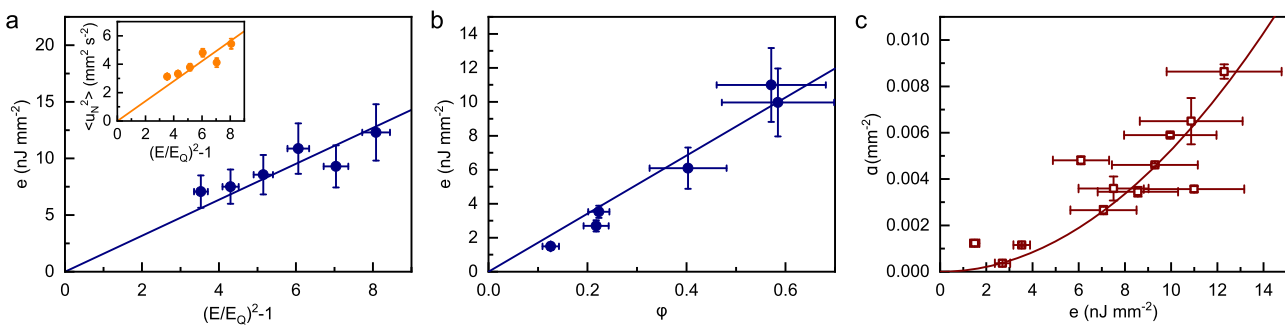


**Fig. 4 Activity enhances droplet shape fluctuations.** **a** The energy per area,  $e$ , dependence on electric field  $E$ ,  $(E/E_Q)^2 - 1$ , with  $E_Q = 1.50 \pm 0.03 \text{ MV m}^{-1}$ . Inset: Linear dependence of the square average of velocity fluctuations  $\langle u_N^2 \rangle$  on  $(E/E_Q)^2 - 1$ . In both cases the line is a least squares fit to the experimental points. All experiments were performed on the same droplet with packing fraction  $\varphi = 0.58 \pm 0.11$  and droplet area  $A_{\text{drop}} = 11.05 \pm 0.03 \text{ mm}^2$ . **b** As predicted by Eq. (2), the energy density  $e$  is linearly dependent on  $\varphi$ . The line is a least squares fit to the experimental points. These experiments were performed at the same  $E = 4.25 \pm 0.01 \text{ MV m}^{-1}$  but different droplets with  $A_{\text{drop}}$  in the range from  $8.97 \text{ mm}^2$  to  $11.25 \text{ mm}^2$ . **c** A graph of the power spectrum slope  $\alpha$ , defined as  $\langle |h_{\text{q}}|^2 \rangle = \alpha q^{-4}$ , versus  $e$  demonstrates a quadratic dependence (red line). The experimental points were obtained from several realizations of the active droplet:  $E$  from  $3.19$  to  $4.52 \text{ MV m}^{-1}$ ;  $\varphi$  from  $0.13$  to  $0.58$ ; and  $A_{\text{drop}}$  from  $8.97$  to  $11.25 \text{ mm}^2$ . Error bars are the standard error of the mean.

$E^{25,54}$ , thus we have an external control over the velocity fluctuations. The  $\langle u_N^2 \rangle$  linearly increases with  $(E/E_Q)^2 - 1$  (see Fig. 4a inset) and, as a result, the energy density  $e$  is proportional to  $(E/E_Q)^2 - 1$  (Fig. 4a). The energy density also follows a linear dependence on the packing fraction  $\varphi$  as predicted by Eq. (2) (Fig. 4b), demonstrating that addition of active agents is directly reflected in increased energy injection into the droplet.

Activity is known to enhance fluctuations of ring polymers<sup>49</sup> and vesicles<sup>55–59</sup>. However in these systems the active particles are located at the interface, while in our system the active particles are in the bulk, and the interface deforms in response to both direct particle collisions and flow due to the collective motion of the rollers. The magnitude of the active shape fluctuations in our system scales as  $\langle |h_{\text{q}}|^2 \rangle = \alpha q^{-4}$  (Fig. 3b), in agreement with the scaling predicted for fluctuations due to particle collisions with a fluid interface governed by surface tension<sup>35</sup>. The active pressure associated with the particle collisions is a volumetric energy density, thus the theory suggests that  $\alpha$  should scale quadratically with the energy density, which is in agreement with our experimental results (Fig. 4c). A quadratic increase of the fluctuations magnitude with activity, quantified by the Peclet number, is also predicted for the ring polymer system<sup>49</sup>. It is intriguing that different systems (e.g., our system is dense and particle motions are strongly correlated, while the model of ref. 35 considers uncorrelated collisions) display qualitatively similar behavior.

**Spontaneous droplet self-propulsion.** The shape fluctuations are accompanied by a motion of the droplet as a whole. The behavior of the mean square displacement (MSD)  $\langle \Delta r^2 \rangle$  for the center of the droplet exhibits a typical diffusive behavior at the long time scales (see Fig. 5a), and it is in agreement with the behavior observed with droplets enclosing bacteria<sup>38</sup> or active nematics<sup>30</sup>, and predicted by simulations for microswimmers in a vesicle<sup>33</sup>. As activity increases, the droplet shape fluctuations grow and the system occasionally undergoes a symmetry-breaking instability. The global vortex spontaneously splits into two counter-rotating entities that drive a significant elongation of the droplet (as illustrated by the changes in the droplet perimeter shown in Fig. 5b and Supplementary Movie 3) along the line connecting the centers of the new vortices. Such events result in bursts of persistent motion of the droplet in a randomly chosen direction reminiscent of the Levy flights. During the vortex pair formations the maximal Feret diameter of the droplet is always perpendicular

to the direction of the droplet travel (corresponding angle to  $\beta \approx \pi/2$ ), see the inset of Fig. 5b) in contrast to the regular droplet excursions that do not show correlations between  $\beta$  and velocity of the droplet (see Supplementary Fig. S1). The droplet translation persist for about 2–3 s after which the vortex pair recombines into the global vortex and the droplet restores its nearly-circular shape. The events of spontaneous splitting of the self-assembled vortex into two entities leading to a droplet elongation and subsequent bursts of self-propulsion are probabilistic and statistically rare compared to the regular behavior but the phenomenon is robust.

## Conclusions

In this work, we experimentally explored the dynamics of motile colloids in soft confinement. We employ Quincke rollers in a droplet as a model system, with the rollers speed easily controlled by the applied field strength. We find that the interplay between deformable confinement and activity-driven flow gives rise to several previously unobserved phenomena. At low activity, the rollers form a vortex spanning the whole droplet, in contrast to rollers in solid-wall confinement, where the particles accumulate near the boundary. The droplet contour fluctuates about a circular shape and the fluctuations power spectrum is consistent with active fluctuations driven by particle-interface collisions. The non-equilibrium nature of the shape fluctuations is revealed by a broken detailed balance of the shape dynamics. While the interface deformation is driven by the particle-induced flow, the relaxation appears mainly controlled by surface tension as evidenced by the time correlations of the shape fluctuations. Shape fluctuations grow with the activity and can result in a spontaneous extension of the droplet in one direction driven by a formation of the vortex doublet. The spontaneous droplet elongations are accompanied by bursts of persistent self-propulsion in a direction perpendicular to the extension axis. The vortex splitting and recovery lasts for few seconds during which time the droplet can travel a distance of several droplet radii. The timing of the excursion and the direction of motion are randomly chosen. Their control requires understanding of the symmetry-breaking mechanism that leads to the vortex doublet formation. Our results provide insights into the complex dynamic behavior of active colloidal suspensions confined by a deformable boundary and provide new directions for future research in the engineering of self-propelled micromachines.

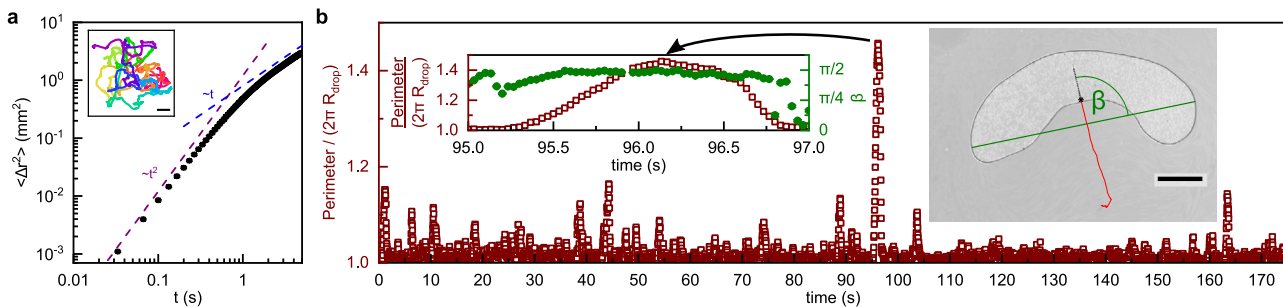


**Fig. 5 Spontaneous droplet self-propulsion.** **a** An example of the experimental mean square displacement for the drop center of mass (MSD) ( $\langle \Delta^2 \rangle$ ). Inset: Trajectory of the droplet center of mass for the duration of experiment. The color progression from red to violet indicates the passage of time. Scale bar is 1 mm. **b** Time series for the droplet perimeter normalized by the equivalent circle perimeter shows surges in droplet deformation accompanied by directed motion. The times series for the asphericity are shown in Supplementary Fig. S2. Inset: A closer inspection reveals that the direction of motion is perpendicular to the maximal caliper diameter defined with an angle  $\beta$  (see inset snapshot, the green line is the obtained maximal caliper (Feret) diameter and the red line is the trajectory up to that moment, Scale bar is 1 mm). Experimental parameters: roller packing fraction  $\varphi = 0.28 \pm 0.02$ , droplet area  $A_{\text{drop}} = 10.07 \pm 0.03 \text{ mm}^2$ , electric field strength  $E = 4.464 \pm 0.008 \text{ MV m}^{-1}$ .

## Methods

**Experimental system.** Spherical polystyrene particles ( $d = 2a = 40 \mu\text{m}$  diameter, Phosphorex) and density  $1.06 \text{ g cm}^{-3}$  in hexadecane ( $\rho_{\text{hexadecane}} = 0.77 \text{ g cm}^{-3}$ ) are dispersed in hexadecane with  $0.1 \text{ mol L}^{-1}$  diethyl sulfosuccinate sodium (AOT) salt (Sigma Aldrich). A small amount of the solution with the particles (approx.  $5 \mu\text{L}$ ) is sandwiched between two indium tin oxide (ITO) coated glass slides to form a liquid bridge with a high aspect ratio. The distance between the electrodes is set by glass spheres with diameter  $150 \mu\text{m}$  (Novum Glass) embedded in vacuum grease. Particles are allowed to sediment on the bottom electrode. We explore several packing fractions  $\varphi$ , ranging from 0.13 to 0.58, of Quincke rollers inside droplets. The packing fraction is determined by a thresholding method described in details in Supplementary Note II.

**Imaging and droplet shape analysis.** The recordings are made with a fast CMOS camera (IDT) at 300 fps and 500 fps mounted on a stereoscope (Leica). Velocity, vorticity fields and streamlines reflect the motion of the Quincke rollers and were obtained by a particle image velocimetry (PIV) package MatPIV for Matlab. Velocity fields together with the movement of the entire liquid bridge served as the input to calculate the energy per unit area  $E_{\text{tot}}/A_{\text{drop}}$  of the system.

To characterize the droplet contour fluctuations each image was automatically thresholded by Otsu's method in Matlab to obtain the border outline. The center of the droplet  $\vec{R}_c$  was determined as the mean coordinates of the droplet area pixels,  $A_{\text{drop}}$ , and equivalent radius was calculated  $R_{\text{drop}} = \sqrt{A_{\text{drop}}/\pi}$ . The perimeter of the equivalent circle with  $R_{\text{drop}}$  around  $\vec{R}_c$  served as the baseline for the coordinate  $s$  and the radial deviations from the equivalent circle  $h(s)$  were determined from the images (Fig. 3a inset). We used the square of the fast Fourier transform algorithm in Matlab to compute the power spectrum of the fluctuations and averaged it over time. The number of frames to calculate the temporal averages of all the measured quantities was  $>2000$ , error bars represent the standard error of the mean value.

The droplet radius of gyration  $R_g$  and asphericity  $\Delta$  were determined by the gyration tensor  $\bar{\bar{Q}} = \frac{1}{N} \sum_{n=1}^N (\vec{R}_n - \vec{R}_c) \otimes (\vec{R}_n - \vec{R}_c)$ , where index  $n$  runs over all area pixels of the liquid bridge drop ( $N$  in total).  $\bar{\bar{Q}}$  has eigenvalues  $\lambda_1$  and  $\lambda_2$  which define  $R_g = \sqrt{\lambda_1 + \lambda_2}$  and  $\Delta = (\lambda_1 - \lambda_2)^2/(\lambda_1 + \lambda_2)^2$ .

**Detailed balance analysis of the shape fluctuations.** The methodology follows ref. 52 to analyze the transitions between microscopic configurations defined as the shapes corresponding to different Fourier modes. We compute the trajectory in the phase space spanned by the two modes from the time series of their amplitudes. Then the phase space is discretized into equally sized, rectangular boxes each of which represents a discrete state. The probability is defined as the ratio of the time spent at a given state and the total trajectory time. The arrows indicate the currents across box boundaries determined by counting transitions between boxes. The transitions between neighboring discrete states occur when the system trajectory crosses box boundaries. Computing the contour integral of the probability current,  $\Omega = \frac{\int_C j \cdot dl}{\int_C |j| dl}$ , shows a non-zero circulation for a system out of equilibrium. Details of the methodology can be found in Supplementary Note III.

## Data availability

The data that support the findings of this study are available from the corresponding author upon reasonable request.

## Code availability

All relevant code used in this study is available from the corresponding author upon reasonable request.

Received: 21 October 2021; Accepted: 22 March 2022;

Published online: 14 April 2022

## References

1. Gompper, G. et al. The 2020 motile active matter roadmap. *J. Phys. Condens. Matter* **32**, 193001 (2020).
2. Tanjeem, N., Minnis, M. B., Hayward, R. C. & Shields, C. W. Shape-changing particles: From materials design and mechanisms to implementation. *Adv. Mater.* **34**, 2105758 (2022).
3. Snejhko, A. & Aranson, I. S. Magnetic manipulation of self-assembled colloidal asters. *Nat. Mater.* **10**, 698–703 (2011).
4. Van Blaaderen, A. et al. Manipulating the self assembly of colloids in electric fields. *Eur. Phys. J. Spec. Top.* **222**, 2895–2909 (2013).
5. Dobnikar, J., Snejhko, A. & Yethiraj, A. Emergent colloidal dynamics in electromagnetic fields. *Soft Matter* **9**, 3693–3704 (2013).
6. Yan, J. et al. Reconfiguring active particles by electrostatic imbalance. *Nat. Mater.* **15**, 1095–1099 (2016).
7. Han, K., Shields IV, C. W. & Velez, O. D. Engineering of self-propelling microbots and microdevices powered by magnetic and electric fields. *Adv. Funct. Mater.* **28**, 1705953 (2018).
8. Han, K. et al. Emergence of self-organized multivortex states in flocks of active rollers. *Proc. Natl. Acad. Sci.* **117**, 9706–9711 (2020).
9. Driscoll, M. & Delmotte, B. Leveraging collective effects in externally driven colloidal suspensions: experiments and simulations. *Curr. Opin. Colloid Interface Sci.* **40**, 42–57 (2019).
10. Han, K. et al. Reconfigurable structure and tunable transport in synchronized active spinner materials. *Sci. Adv.* **6**, eaaz8535 (2020).
11. Palacci, J., Sacanna, S., Steinberg, A. P., Pine, D. J. & Chaikin, P. M. Living crystals of light-activated colloidal surfers. *Science* **339**, 936–940 (2013).
12. Vutukuri, H. R., Lisicki, M., Lauga, E. & Vermant, J. Light-switchable propulsion of active particles with reversible interactions. *Nat. Commun.* **11**, 1–9 (2020).
13. Paxton, W. F. et al. Catalytic nanomotors: autonomous movement of striped nanorods. *J. Am. Chem. Soc.* **126**, 13424–13431 (2004).
14. Howse, J. R. et al. Self-motile colloidal particles: from directed propulsion to random walk. *Phys. Rev. Lett.* **99**, 048102 (2007).
15. Popescu, M. N., Uspal, W. E., Domínguez, A. & Dietrich, S. Effective interactions between chemically active colloids and interfaces. *Acc. Chem. Res.* **51**, 2991–2997 (2018).
16. Dombrowski, C., Cisneros, L., Chatkaew, S., Goldstein, R. E. & Kessler, J. O. Self-concentration and large-scale coherence in bacterial dynamics. *Phys. Rev. Lett.* **93**, 098103 (2004).
17. Sokolov, A., Aranson, I. S., Kessler, J. O. & Goldstein, R. E. Concentration dependence of the collective dynamics of swimming bacteria. *Phys. Rev. Lett.* **98**, 158102 (2007).
18. Wensink, H. H. et al. Meso-scale turbulence in living fluids. *Proc. Natl. Acad. Sci.* **109**, 14308–14313 (2012).

19. Dunkel, J. et al. Fluid dynamics of bacterial turbulence. *Phys. Rev. Lett.* **110**, 228102 (2013).

20. Wieland, H., Woodhouse, F. G., Dunkel, J. & Goldstein, R. E. Ferromagnetic and antiferromagnetic order in bacterial vortex lattices. *Nat. Phys.* **12**, 341–345 (2016).

21. Theillard, M., Alonso-Matilla, R. & Saintillan, D. Geometric control of active collective motion. *Soft Matter* **13**, 363–375 (2017).

22. Nishiguchi, D., Aranson, I. S., Snezhko, A. & Sokolov, A. Engineering bacterial vortex lattice via direct laser lithography. *Nat. Commun.* **9**, 1–8 (2018).

23. Wieland, H., Woodhouse, F. G., Dunkel, J., Kessler, J. O. & Goldstein, R. E. Confinement stabilizes a bacterial suspension into a spiral vortex. *Phys. Rev. Lett.* **110**, 268102 (2013).

24. Lushi, E., Wieland, H. & Goldstein, R. E. Fluid flows created by swimming bacteria drive self-organization in confined suspensions. *Proc. Natl Acad. Sci.* **111**, 9733–9738 (2014).

25. Bricard, A., Caussin, J.-B., Desreumaux, N., Dauchot, O. & Bartolo, D. Emergence of macroscopic directed motion in populations of motile colloids. *Nature* **503**, 95–98 (2013).

26. Bricard, A. et al. Emergent vortices in populations of colloidal rollers. *Nat. Commun.* **6**, 1–8 (2015).

27. Tjhung, E., Marenduzzo, D. & Cates, M. E. Spontaneous symmetry breaking in active droplets provides a generic route to motility. *Proc. Natl Acad. Sci.* **109**, 12381–12386 (2012).

28. Singh, D. P. et al. Interface-mediated spontaneous symmetry breaking and mutual communication between drops containing chemically active particles. *Nat. Commun.* **11**, 1–8 (2020).

29. Gao, T. & Li, Z. Self-driven droplet powered by active nematics. *Phys. Rev. Lett.* **119**, 108002 (2017).

30. Sanchez, T., Chen, D. T., DeCamp, S. J., Heymann, M. & Dogic, Z. Spontaneous motion in hierarchically assembled active matter. *Nature* **491**, 431–434 (2012).

31. Zwicker, D., Seyboldt, R., Weber, C. A., Hyman, A. A. & Juelicher, F. Growth and division of active droplets provides a model for protocells. *Nat. Phys.* **13**, 408–413 (2017).

32. Vutukuri, H. R. et al. Active particles induce large shape deformations in giant lipid vesicles. *Nature* **586**, 52–56 (2020).

33. Paoluzzi, M., Di Leonardo, R., Marchetti, M. C. & Angelani, L. Shape and displacement fluctuations in soft vesicles filled by active particles. *Sci. Rep.* **6**, 34146 (2016).

34. Li, Y. & ten Wolde, P. R. Shape transformations of vesicles induced by swim pressure. *Phys. Rev. Lett.* **123**, 148003 (2019).

35. Takatori, S. C. & Sahu, A. Active contact forces drive nonequilibrium fluctuations in membrane vesicles. *Phys. Rev. Lett.* **124**, 158102 (2020).

36. Chen, J., Hua, Y., Jiang, Y., Zhou, X. & Zhang, L. Rotational diffusion of soft vesicles filled by chiral active particles. *Sci. Rep.* **7**, 1–12 (2017).

37. Abaurrea-Velasco, C., Auth, T. & Gompper, G. Vesicles with internal active filaments: self-organized propulsion controls shape, motility, and dynamical response. *N. J. Phys.* **21**, 123024 (2019).

38. Ramos, G., Cordero, M. L. & Soto, R. Bacteria driving droplets. *Soft Matter* **16**, 1359–1365 (2020).

39. Huang, Z., Omori, T. & Ishikawa, T. Active droplet driven by a collective motion of enclosed microswimmers. *Phys. Rev. E* **102**, 022603 (2020).

40. Rajabi, M., Baza, H., Turiv, T. & Lavrentovich, O. D. Directional self-locomotion of active droplets enabled by nematic environment. *Nat. Phys.* **17**, 260–266 (2021).

41. Karani, H., Pradillo, G. E. & Vlahovska, P. M. Tuning the random walk of active colloids: From individual run-and-tumble to dynamic clustering. *Phys. Rev. Lett.* **123**, 208002 (2019).

42. Zhang, B., Sokolov, A. & Snezhko, A. Reconfigurable emergent patterns in active chiral fluids. *Nat. Commun.* **11**, 1–9 (2020).

43. Tsebers, A. Internal rotation in the hydrodynamics of weakly conducting dielectric suspensions. *Fluid Dyn.* **15**, 245–251 (1980).

44. Kokot, G. & Snezhko, A. Manipulation of emergent vortices in swarms of magnetic rollers. *Nat. Commun.* **9**, 1–7 (2018).

45. Wang, Y., Canic, S., Kokot, G., Snezhko, A. & Aranson, I. Quantifying hydrodynamic collective states of magnetic colloidal spinners and rollers. *Phys. Rev. Fluids* **4**, 013701 (2019).

46. Brochard, F. & Lennon, J. Frequency spectrum of the flicker phenomenon in erythrocytes. *J. de Phys.* **36**, 1035–1047 (1975).

47. Granek, R. From semi-flexible polymers to membranes: anomalous diffusion and reptation. *J. de Phys. II* **7**, 1761–1788 (1997).

48. Finken, R., Lamura, A., Seifert, U. & Gompper, G. Two-dimensional fluctuating vesicles in linear shear flow. *Eur. Phys. J. E* **25**, 309–321 (2008).

49. Mousavi, S. M., Gompper, G. & Winkler, R. G. Active brownian ring polymers. *J. Chem. Phys.* **150**, 064913 (2019).

50. De Gennes, P.-G. Wetting: statics and dynamics. *Rev. Mod. Phys.* **57**, 827 (1985).

51. Ondarcuhu, T. & Veyssié, M. Relaxation modes of the contact line of a liquid spreading on a surface. *Nature* **352**, 418–420 (1991).

52. Battle, C. et al. Broken detailed balance at mesoscopic scales in active biological systems. *Science* **352**, 604–607 (2016).

53. Goldhirsch, I. Introduction to granular temperature. *Powder Technol.* **182**, 130–136 (2008).

54. Pradillo, G. E., Karani, H. & Vlahovska, P. M. Quincke rotor dynamics in confinement: rolling and hovering. *Soft Matter* **15**, 6564–6570 (2019).

55. Manneville, J.-B., Bassereau, P., Levy, D. & Prost, J. Activity of transmembrane proteins induces magnification of shape fluctuations of lipid membranes. *Phys. Rev. Lett.* **82**, 4356 (1999).

56. Manneville, J.-B., Bassereau, P., Ramaswamy, S. & Prost, J. Active membrane fluctuations studied by micropipet aspiration. *Phys. Rev. E* **64**, 021908 (2001).

57. Girard, P., Prost, J. & Bassereau, P. Passive or active fluctuations in membranes containing proteins. *Phys. Rev. Lett.* **94**, 088102 (2005).

58. Loubet, B., Seifert, U. & Lomholt, M. A. Effective tension and fluctuations in active membranes. *Phys. Rev. E* **85**, 031913 (2012).

59. Turlier, H. & Betz, T. Unveiling the active nature of living-membrane fluctuations and mechanics. *Annu. Rev. Condens. Matter Phys.* **10**, 213–232 (2019).

## Acknowledgements

A.S. and G.K. were supported by the U.S. Department of Energy, Office of Science, Basic Energy Sciences, Materials Sciences and Engineering Division. P.M.V. was supported by NSF-DMR award 2004926.

## Author contributions

A.S., P.M.V., and G.K. designed the research. G.K. performed the experiments and analyzed the data. H.F. performed the analysis of the shape fluctuations. G.E.P. obtained the preliminary results and discovered the crawling drop phenomenon. A.S., H.F., P.M.V., and G.K. wrote the paper.

## Competing interests

The authors declare no competing interests.

## Additional information

**Supplementary information** The online version contains supplementary material available at <https://doi.org/10.1038/s42005-022-00872-9>.

**Correspondence** and requests for materials should be addressed to Petia M. Vlahovska.

**Peer review information** *Communications Physics* thanks the anonymous reviewers for their contribution to the peer review of this work. Peer reviewer reports are available

**Reprints and permission information** is available at <http://www.nature.com/reprints>

**Publisher's note** Springer Nature remains neutral with regard to jurisdictional claims in published maps and institutional affiliations.



**Open Access** This article is licensed under a Creative Commons Attribution 4.0 International License, which permits use, sharing, adaptation, distribution and reproduction in any medium or format, as long as you give appropriate credit to the original author(s) and the source, provide a link to the Creative Commons license, and indicate if changes were made. The images or other third party material in this article are included in the article's Creative Commons license, unless indicated otherwise in a credit line to the material. If material is not included in the article's Creative Commons license and your intended use is not permitted by statutory regulation or exceeds the permitted use, you will need to obtain permission directly from the copyright holder. To view a copy of this license, visit <http://creativecommons.org/licenses/by/4.0/>.

© The Author(s) 2022